of the high-temperature structural modifications of iron between 30 and 60 GPa. Funamori *et al.* (*17*) found γ iron to be stable up to 32 GPa and 1500 K. Saxena *et al.* (*4, 12*) suggested that iron underwent a phase transformation to β phase with δ hcp structure at 40 to 60 GPa. They recorded x-ray patterns on quenched samples previously heated with intentionally strong temperature gradients [see figure 2 in (*12*)]. In such an experimental procedure, samples were most likely subjected to strong stress fields that might bias structural determinations. Dubrovinsky *et al.* (*18*) recently provided experimental data supporting a δ hcp structure. The major evidence was the presence of 004 and 103 Bragg lines, which however disappeared with prolonged heating; thus raising the possibility that the reflections were from an unstable intermediate iron structure. Yoo *et al.* (*5*) recognized a metastable new polymorph at lower pressures and located it within the previously defined γ iron stability field. They did not observe a phase transformation when laser heating ε iron between 40 and 60 GPa. The absence of a phase transformation in this range disagrees with the other reports (*2–4*) and our study.

All of our spectra recorded at high-temperatures from 30 to 60 GPa and at 100 GPa correspond to the described orthorhombic lattice. The stability field of this polymorph thus appears similar to that proposed by Saxena *et al.* (*4*) for the β phase. We believe that the main difference between their study and our work lies in the interpretation of the diffraction patterns, and thus propose that the structure of the β phase is the orthorhombic lattice. From our results, it appears that the stability field of γ iron should not extend much above 32 GPa, while that of β iron extends up to at least 100 GPa (Fig. 6).

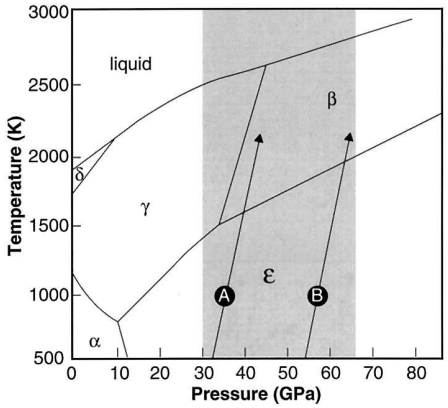

Fig. 6. Revised pressure-temperature phase diagram of iron [derived from (*12*)]. The A and B arrows are an estimate of the pressure-temperature path of iron during laser heating under pressure. We maintain β iron as a name for the newly determined orthorhombic structure. Melting curve was determined by Boehler *et al.* and Shen *et al.* (*3,19*). Persistence of the γ phase at 32 GPa and 1500 K was indicated by in situ x-ray experiments (*17*).

REFERENCES AND NOTES

1. O. L. Anderson and A. Duba, *J. Geophys. Res.*, in press.
2. J. M. Brown and R. G. McQueen, *ibid.* **91**, 7485 (1986).
3. R. Boehler, *Geophys. Res. Lett.* **13**, 1153 (1986); *Nature* **363**, 534 (1993).
4. S. K. Saxena, G. Shen, P. Lazor, *Science* **260**, 1312 (1993); S. K. Saxena *et al.*, *ibid.* **269**, 1703 (1995).
5. C. S. Yoo, J. Akella, A. J. Campbell, H. K. Mao, R.J. Hemley, *ibid.* **270**, 1473 (1995).
6. G. Fiquet *et al.*, *Phys. Earth Planet. Inter.*, in press.
7. See (*6*) for details of the experimental setup [G. Shen and P. Lazor, *J. Geophys. Res.* **100**, 17699 (1995)].
8. As mentioned in previous reports [D. L. Heinz, *Geophys. Res. Lett.* **17**, 1161 (1990); see (*6*)], the pressure slightly increases within the laser hot spot. We estimated a correction, and we will not further discuss such effects.
9. J. C. Chervin, B. Canny, P. Pruzan, *Rev. Sci. Instrum.* **66**, 2595 (1995).
10. D. Haüsermann and M. Hanfland, *High Press. Res.* **14**, 223 (1996).
11. J. Hammersley, *ESRF publication* (1996).
12. S. K. Saxena, L. S. Dubrowinski, P. Häggkvist, *Geophys. Res. Lett.* **23**, 2441 (1996).
13. H. K. Mao, Y. Wu, L. C. Chen and J. F. Shu, *J. Geophys. Res.* **95**, 21737 (1990).
14. A similar flexibility was also reported for the ε iron lattice when coexisting with α iron [E. Huang, W. A. Basset, P. Tao, in *High-Pressure Research in Mineral Physics*, M. H. Manghnani and Y. Syono, Eds. (American Geophysical Union, Washington, DC, 1987), pp. 165–172].
15. The pressure is calculated from the 110 Bragg line of SiO_2 found at 2.754 Å, and according to the compression curve presented by Y. Tsuchida and T. Yagi [*Nature* **340**, 217 (1989)]. The SiO_2 diffraction features were satisfactorily reproduced using the stishovite indexation, and volume was calculated to be 38.090 $Å^3$.
16. A. LeBail, in *Accuracy in Powder Diffraction*, E. Prince and J. K. Stalick, Eds., (NIST, Maryland, 1992), p. 213; A. C. Larson and R. B. Von Dreele, *Los Alamos National Laboratory LAUR publication* (1994).
17. N. Funamori, T. Yagi, T. Uchida, *Geophys. Res. Lett.* **23**, 953 (1996).
18. L. S. Dubrovinsky, S. K. Saxena, P. Lazor, *ibid.* **24**, 1835 (1997).
19. R. Boehler, N. Von Bargen, A. Chopelas, *J. Geophys. Res.* **95**, 21731 (1990); G. Shen, P. Lazor, S. K. Saxena, *Phys. Chem. Min.* **20**, 91 (1993).

20. We thank S. Bauchau, J. Peyronneau, R. Visocekas for experiments; F. Guyot, M. Hanfland, J. P. Poirier for discussions; C. McCammon and J. Hohl for corrections; W. A. Basset, O. L. Anderson, and anonymous reviewers for comments; and Jibidouille for graphics. This work was initiated from collaboration with P. Richet and P. Gillet and supported by Dynamique et Bilan de la Terre II.

10 June 1997; accepted 6 October 1997

Three-Dimensional Dynamic Simulation of the 1992 Landers Earthquake

K. B. Olsen,* R. Madariaga, R. J. Archuleta

The 1992 Landers, California, earthquake (magnitude 7.3) was modeled as the propagation of a spontaneous rupture controlled by a realistic prestress distribution with the use of a three-dimensional finite-difference method. The dynamic rupture reproduces the general slip pattern used to compute the initial stress distribution and generates near-fault ground motions at the surface similar to observations. The simulated rupture propagates on the fault along a complex path with highly variable speed and rise time, changing the magnitude and pattern of the stress significantly. The method provides the framework to estimate earthquake rupture parameters from recorded seismic and geodetic data.

The rupture of earthquakes and the resulting ground shaking have usually been studied from two complementary but different perspectives. The rupture is typically analyzed by seismologists interested in the initiation, propagation, and healing of earthquake ruptures using complicated models (*1, 2*), whereas the resulting ground shaking is generally computed in specific areas on the basis of a simple kinematic definition of the source (*3*). Here, we combine the two efforts into a single integrated approach, including the computational efficiency of recent kinematic methods (*4*). We assume rupture on a planar, vertical fault, although it would be possible in principle to simulate more complex ruptures.

The main assumption in seismic source dynamics is that traction and slip, the relative displacement of one side of the fault with respect to the other, are related by a friction law across the fault zone. This friction law is a function of local rupture parameters including slip (**D**), slip rate ($\dot{\mathbf{D}}$), and certain state variables (*5*) that describe the aging of fault contacts, fluid pressure, temperature, and several other slowly vary-

K. B. Olsen and R. J. Archuleta, Institute for Crustal Studies, University of California, Santa Barbara, CA 93106–1100, USA.
R. Madariaga, Laboratoire de Géologie, Ecole Normale Supérieure, 24 rue Lhomond, 75231 Paris Cedex 05, France.
*To whom correspondence should be addressed.

ing properties of the fault. The total traction **T**, and therefore friction, on the fault can be expressed as the sum of a preexisting stress field $\mathbf{T}^0$ and the stress change $\Delta\mathbf{T}$ due to slip on the fault

$$\mathbf{T}(\mathbf{D}, \dot{\mathbf{D}}, \theta) = \mathbf{T}^0 + \Delta\mathbf{T} \qquad (1)$$

where θ refers to possible state variables. Prestress $\mathbf{T}^0$ is generated by a combination of tectonic loads caused by plate motion and internal deformation and the residual stresses from earlier seismic events on the fault and its vicinity. We modeled a single event, assuming that the prestress is known. The change in traction $\Delta\mathbf{T}$ is related through the solution of the wave equation to the history of slip on the fault.

We used a fourth-order staggered-grid, finite-difference solution to the three-dimensional elastic wave equation (*6*) to compute the stress change for a given slip history on the fault. Our scheme includes a free-surface boundary condition at the top and sponge layers (*7*) in addition to absorbing boundary conditions (*8*) at the remaining grid boundaries. The use of fourth-order, spatially accurate derivatives in the finite-difference scheme ensures that all stresses and velocities have the appropriate symmetries about the fault plane (*9*). This property reduces many of the numerical instabilities that have prevented accurate simulations of fault dynamics by the use of finite-difference methods (*10*).

We used a friction law for which slip is zero until the total stress reaches a critical yield value ($\mathbf{T}_u$). Once this stress has been attained, slip rate (and therefore slip) increases rapidly from zero while traction across the fault decreases to zero (*11*),

$$\mathbf{T}(\mathbf{D}) = \mathbf{T}_u\left[1 - \frac{|\mathbf{D}|}{D_0}\right] \text{ for } |\mathbf{D}| < D_0$$

$$\mathbf{T}(\mathbf{D}) = 0 \qquad \text{for } |\mathbf{D}| > D_0 \qquad (2)$$

Here D_0 is the so-called slip-weakening distance. The decrease of friction **T** with increasing slip $|\mathbf{D}|$ is a universal property that is necessary for the friction law to be dissipative (*12*). If slip weakening is omitted, stress becomes infinite at the rupture front so that, after a numerical transient, seismic ruptures would continue propagating forever at exactly the terminal rupture velocity. The most important feature introduced by this friction law is a characteristic length D_0 that defines a minimum size for a stable rupture zone (*13*).

Although friction is a vector property, we assumed that slip occurs only in the direction parallel to the applied shear stress. In this way, slip becomes a scalar ($D = |\mathbf{D}|$) in the simulations and reduces the number of rupture parameters needed in the model (*14*). This assumption is consistent with kinematic source inversion results (*15*) and recent numerical experiments (*16*) suggesting that slip is predominantly aligned with the shear prestress, along the long dimension of a shallow strike-slip fault (simple shear).

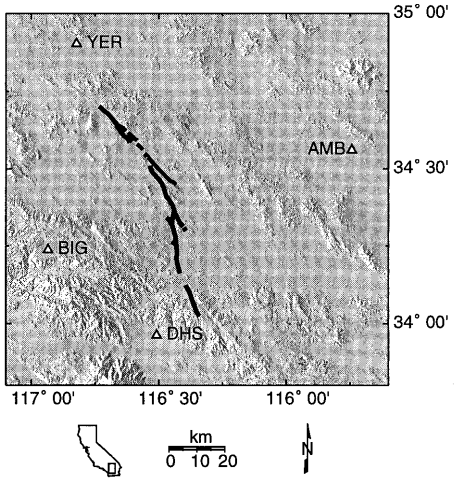

Fig. 1. Topographic map showing the surface rupture from the 1992 Landers earthquake. The fault trace is depicted by the black lines, and the triangles depict the location of stations at which we compared our modeling result with recorded seismograms.

The 28 June 1992 Landers earthquake (magnitude 7.3) occurred in a remote area of the Mojave Desert in southern California (Fig. 1), but the rupture process has been extensively studied (*17*) because of its large size, proximity to the southern California metropolitan areas, and wide coverage by seismic instruments. Several studies inverted for the rupture history of this event from a combination of seismograms, geodetic data, and geologic data (*18–20*). The overall kinematics of the seismic rupture are thought to be understood (*18–20*), making the Landers earthquake an appropriate test case for our dynamic modeling method.

The fault that ruptured during the Landers earthquake can be divided into three segments: the Landers–Johnson Valley (LJV) segment to the southeast, where the hypocenter was located; the Homestead Valley (HV) segment in the central part of the fault; and the Camp Rock–Emerson (CRE) segment to the northwest. For the numerical simulation, we replaced the three segments of the fault by a single 78-km-long vertical fault plane extending from the surface down to a depth of 15 km.

The most important parameter required for dynamic modeling is the initial stress on the fault before rupture starts; all other observable characteristics of the seismic rupture, including the motion of the rupture front, are determined by the friction law. To estimate the initial stress field, we used the slip distribution for the Landers earthquake proposed by Wald and Heaton (*18*). From this slip distribution, we computed the change in static traction along the longitudinal direction of the fault using our finite-difference method. We then reversed the sign of this stress change and added a constant "tectonic stress" of 50 bars in order to produce the initial stress field $\mathbf{T}^0$ on the Landers fault (*21, 22*). Thus, the initial stress field ($\mathbf{T}^0$ in Eq. 1) is the sum of internal stresses on the fault due to preslip and previous earthquakes, plus some external spatially uniform tectonic load.

Now that we have defined the initial stress, we need to specify the friction law. The values of the yield stress determining the initiation of slip and the slip weakening distance D_0, which must be a fraction of the slip on the fault (*21*), are more or less unconstrained and may vary on the fault. The general effect of an increase in yield stress and the slip-weakening parameter is to increase rupture resistance. For the moment, D_0 remains unconstrained, although a recent study of the 1995 Kobe earthquake in Japan has proposed rather large values for D_0 (*23*). Because of the lack of constraints, we used a constant value of D_0 even though any distribution of the parameter is allowed by our method. We found that a constant yield stress level of 120 bars and D_0 equal to 80 cm produce a total rupture time and final slip distribution in agreement with kinematic inversion results. Before the simulation, we constrained the initial stress $\mathbf{T}^0$ on the fault to values just below the specified yield level (120 bars) to prevent rupture from several locations. We adopted the same regional one-dimensional (1D) model of velocities and densities as used in (*18*) in our numerical simulations (Tables 1 and 2).

Table 1. Three-dimensional modeling parameters.

Spatial discretization (m)	200
Temporal discretization (s)	0.013
Yield stress (bars)	120
Fault length (km)	78
Fault width (km)	15
Slip-weakening parameter (m)	0.8

Table 2. One-dimensional earth structure and parameters; V_P, *P*-wave velocity; V_S, *S*-wave velocity.

V_P (km/s)	V_S (km/s)	Density (g/cm^3)	Thickness (km)	Depth (km)
3.80	1.98	2.30	1.50	1.50
5.50	3.15	2.60	2.50	4.00
6.20	3.52	2.70	22.0	26.0
6.80	3.83	2.87	6.00	32.0

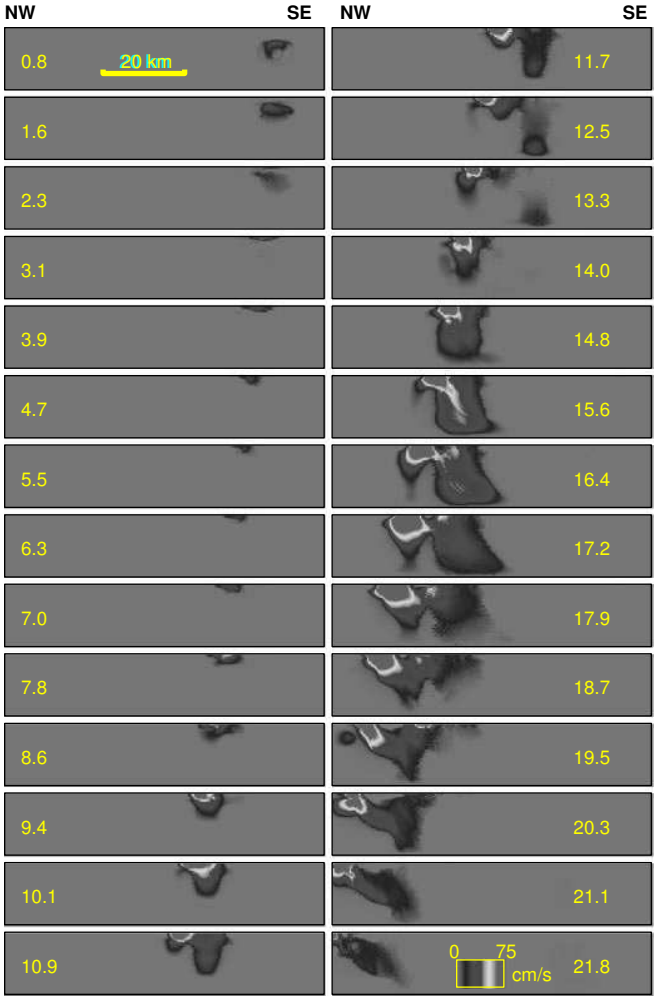

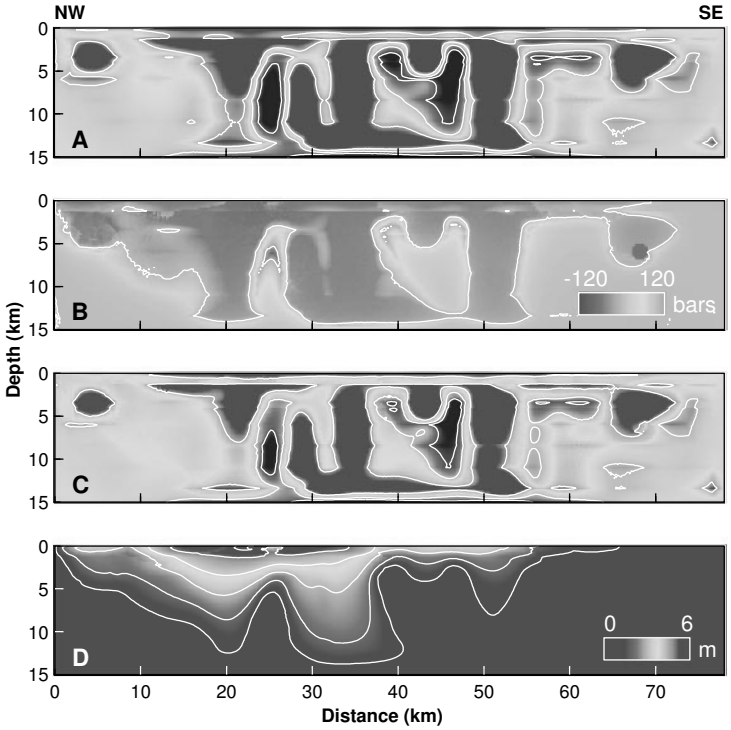

Fig. 2 (**left**). Snapshots of our dynamic rupture simulation of the Landers earthquake on the fault plane. The snapshots depict the horizontal slip rate. **Fig. 3** (**right**). (**A**) Initial stress, (**B**) final stress, (**C**) stress drop, and (**D**) final slip distribution from the dynamic rupture simulation. Contours shown for (A) through (C) are −120, 0, and +120 bars; the contour interval for (D) is 1 m, with the first contour at 1 m.

The initiation of rupture was forced by a lowering of the yield stress in a small patch of radius 1 km inside a high-stress region near the hypocenter toward the southern end of the LJV fault strand, as inferred from the kinematic results (Fig. 2). Soon after initiation, the rupture slows down as a result of the relatively low stress surrounding the initial asperity and shrinks to a small patch of slip near the surface (see snapshots between 3.1 and 7 s, Fig. 2). Then the rupture enters a high-stress area (7.8 s) about 50 km from the northwestern edge. At this point, the rupture becomes more complex. Part of the rupture propagates vertically down and stops (7.8 to 13.3 s, Fig. 2), while another part moves laterally close to the surface. The main part of the rupture moves ahead in the general rupture direction where its strength increases, and it enters a high-stress area about 35 km from the northwestern edge of the fault, representing the HV fault segment. After 14.8 s, the rupture spreads to the full width of the fault with the highest intensity near the surface. Here, the rupture pulse resembles the fast, almost instantaneous self-healing phase with a finite slip duration proposed by Heaton (*24*) for large earthquakes. At 15.6 s, the rupture enters the CRE segment of the fault, where the rupture extends to greater depths as it propagates with a "tail" of slowly healing fault material left behind. Toward the northwestern edge of the fault, the rupture leaps ahead for the last time (18.7 s) onto a smaller patch of higher stressed material near the surface. After about 22 s, the rupture loses energy and terminates near the upper northwestern corner of the fault.

The earthquake has effectively released the stress on all the most heavily loaded areas of the fault (Fig. 3, A through C). The stress has increased within and particularly near the edges of the areas that showed little or no slip (for example, about 25 to 27 km and 37 to 48 km from the northwestern edge of the fault at a depth of 3 to 12 km) to values similar to or larger than the yield stress specified for the earthquake that just occurred. This result has, to our knowledge, not been reported in earlier studies and suggests that these areas could be the locations of nucleation for a future earthquake on the fault. The final slip distribution (maximum 6.1 m) represents a smooth version of the one (*18*) used to compute the initial stress (Fig. 3D).

There are important similarities and differences between the kinematic inversion results (*18*–*20*) and our dynamic reconstruction of the Landers event. Both methods find that a confined rupture pulse generally propagates unilaterally along a continuous path on the fault. A more detailed comparison of the rupture pulse is complicated by the relatively lower resolution of the kinematic inversion. The rupture velocity shows a strong variation during the earthquake for the dynamic simulation (Fig. 4A). On average, the rupture here propagates with velocities close to the local S-wave speed and terminates about 22 s after initiation, in agreement with the kinematic results (*18*–*20*). However, the rupture velocity varies from subsonic to supersonic during the simulation. The subsonic rupture velocities generally occur within and near the low-stress areas on the fault, whereas the supersonic ones dominate within highly stressed patches of the fault where the rupture resistance is relatively low. Supersonic

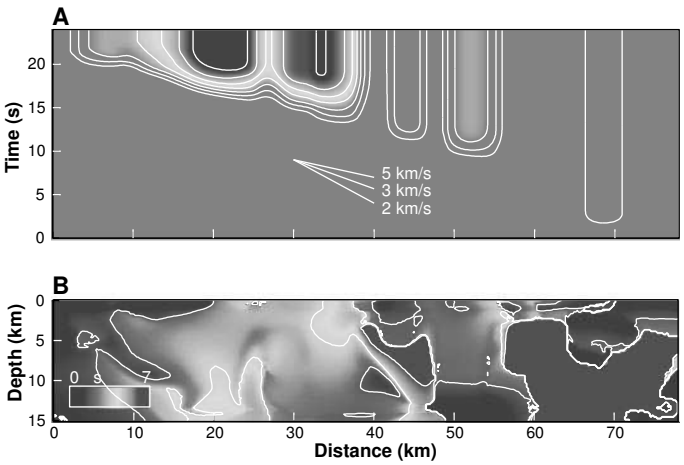

Fig. 4. (**A**) Image and contour plot of the slip rate averaged over a 2-km-wide horizontal band intersecting the hypocenter. Lines depicting a range of rupture velocities are superimposed for comparison. The contour interval is 25 cm for slip between 25 and 175 cm. (**B**) Image and contour plot of the rise times; contours shown are 2, 4, and 6 s.

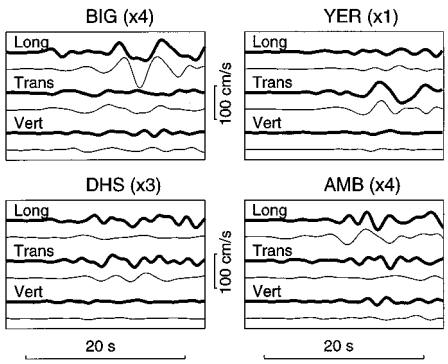

Fig. 5. Comparison of simulated (thin lines) to observed (thick lines) seismograms at four stations (see locations in Fig. 1). Long, Trans, and Vert depict longitudinal, transversal, and vertical components, respectively. Amplitude scaling factors listed at the station abbreviation have been applied to each pair of simulated and observed seismograms. Both simulations and observations are shown within a bandwidth of 0.1 to 0.5 Hz.

velocities are particularly dominating near the surface, allowing the shallow fault to lead the rupture. This result is not expected from the kinematic inversions where the rupture generally propagates faster at depth (*18*). These shallow supersonic rupture velocities are likely caused by the free surface, which promotes the generation of *S* to *P* converted head waves (*S**) (*25*).

The existence of supersonic rupture velocities has been documented in earlier rupture models (*26*), but evidence from seismic data (*27*) is sparse, perhaps because of the limited resolution of the inversion methods. The nearly horizontal time-distance contours in certain areas on the fault represent "jumps" into areas of higher stress (for example, at 4 to 10 km in Fig. 4A and snapshots at 18.7 to 19.5 s in Fig. 2). In addition to promoting supersonic velocities, the free surface enhances the slip and slip rate near the surface, in agreement with earlier dynamic earthquake modeling results (*28*). Rise times, calculated as the time required to accumulate from 10% to 90% of the total slip, are larger in areas of relatively low stress, where the rupture slows down as a result of increased rupture resistance. The pattern and magnitude of the rise times (Fig. 4B) agree with kinematic results (*19*). The resolution of the rise times varies, with the lowest values in the areas where the least amount of slip occurred.

Our model of the rupture process can be compared with observations to determine how the model fits the more complex real event. We have compared the synthetic seismograms generated by our model with the observed velocity seismograms at four stations located in the forward [Yermo (YER)] and backward [Desert Hot Springs (DHS)] rupture directions, as well as southwest [Big Bear Lake (BIG)] and northeast [Amboy (AMB)] of the fault (Figs. 1 and 5). Both synthetic and observed seismograms are bandpass-filtered to frequencies between 0.1 and 0.5 Hz, and the horizontal ground motion is rotated to the approximate longitudinal (154°) and transverse (64°) directions of the simulation. The main features of the low-frequency ground motion for both amplitude and wave form are reproduced by the synthetic seismograms at the four stations. The best fit is obtained for the relatively stronger ground motion recorded in the forward rupture direction (YER). The fit at the other three stations is worse; this is due in part to the weaker ground motion in the back-rupture direction where the relative influence of the crustal structure and fault geometry is larger. Effects of deviations of the simple 1D model are furthermore increased by the large distance from the fault to AMB (65 km). Unfortunately, AMB is the only station available at northeastern azimuths from the fault.

Besides the initial distribution of stress, the only constraint of our rupture model is given by the friction parameters that are not measured. For our Landers simulation, we used only two such parameters, the slip-weakening distance D_0 and the yield stress level. The values of these parameters were selected from a few sensitivity simulations. For instance, the rupture speed and healing of the fault are critically determined by the level of the yield stress and D_0. If D_0 is chosen to be less than about 60 to 80 cm, the rupture duration and therefore the rise times are much shorter than those obtained from kinematic inversion (*18–20*); larger values of D_0 together with a yield stress higher than about 120 bars introduce rupture resistance at a level that prevents the rupture from propagating at all. Although the rupture duration and rise times are strongly related to D_0, the final slip distribution remains practically unchanged for constant values of D_0 that allow rupture propagation. It is presently unclear whether a spatially varying slip-weakening parameter or a slip-rate–dependent friction law (or both) is needed. Thus, we realize that the friction parameters are somewhat unconstrained. However, we believe that our numerical method provides a framework to constrain these parameters by inversion of observed seismic and geodetic data.

REFERENCES AND NOTES

1. An excellent reference to earthquake dynamics is the monograph by B. Kostrov and S. Das [*Principles of Earthquake Source Mechanics* (Cambridge Univ. Press, Cambridge, UK, (1989)].
2. The relation between faulting, fracture, and friction is discussed by C. Scholz [*The Mechanics of Earthquake and Faulting* (Cambridge Univ. Press, Cambridge, UK, 1989)].
3. K. Aki, *J. Geophys. Res.* **73**, 5359 (1968); N. Haskell, *Bull. Seismol. Soc. Am.* **59**, 865 (1969); M. Bouchon, *ibid.* **68**, 1555 (1978); R. Archuleta and S. Day, *ibid.* **70**, 671 (1980); S. Hartzell and D. Helmberger, *ibid.* **72**, 571 (1982).
4. K. Olsen, R. Archuleta, J. Matarese, *Science* **270**, 1628 (1995); K. Olsen and R. Archuleta, *Bull. Seismol. Soc. Am.* **86**, 575 (1996).
5. The nature of the friction that applies to an active fault is a major subject of research [J. Dieterich, *J. Geophys. Res.* **84**, 2161 (1979); *Am. Geophys. Union Geophys. Monogr. Ser.* **24**, 103 (1981); J. Rice and A. Ruina, *Trans. ASME J. Appl. Mech.* **50**, 343 (1983); A. Ruina, *J. Geophys. Res.* **88**, 10359 (1983)]. In this work, we have used a friction law with slip weakening but no rate dependence.
6. The staggered-grid, finite-difference method was first introduced by R. Madariaga [*Bull. Seismol. Soc. Am.* **66**, 639 (1976)] and later analyzed by, among others, J. Virieux [*Geophysics* **49**, 1933 (1984); *ibid.* **51**, 889 (1986)], A. Levander [*ibid.* **53**, 1425 (1988)], and K. Olsen [thesis, University of Utah (1994)].
7. C. Cerjan, D. Kosloff, R. Kosloff, and M. Reshef [*Geophysics* **50**, 705 (1985)] showed that the postulation of a zone (sponge) of artificial attenuation near the grid edges helps eliminate numerical artifacts. In our simulation, we found that a 20-point-wide sponge zone satisfactorily eliminated the artifacts.
8. Clayton-Engquist A1 boundary conditions [R. Clayton and B. Engquist, *Bull. Seismol. Soc. Am.* **67**, 1529 (1977)].
9. The actual numerical implementation in a fourth-order scheme is more complex, making use of the

symmetries in the finite-difference grid. For example, the fault-parallel components of the velocity as well as the normal and σ_{xz} shear stresses are antisymmetric, whereas the fault-perpendicular component of the velocity and the σ_{yx} and σ_{yz} stresses are symmetric across a vertical fault in the *xz* plane. By careful examination of the numerical implementation, it can be shown that, if the numerical values of the velocity and stress have the aforementioned symmetries about the fault plane at the *N*th time step, then they do at upgraded ($N + 1$)th time step as well. Details of the numerical application of the boundary conditions are described in (*16*).
10. J. Virieux and R. Madariaga, *Bull. Seismol. Soc. Am.* **72**, 345 (1982).
11. Slip-weakening friction laws similar to Eq. 2 have been extensively studied by rock mechanicists in Japan; see, for example, M. Ohnaka, Y. Kuwahara, and K. Yamamoto [*Tectonophysics* **144**, 109 (1987)], M. Ohnaka [*Proc. Natl. Acad. Sci. U.S.A.* **93**, 3795 (1996)], and M. Matsu'ura, H. Kataoka, and B. Shibazaki [*Tectonophysics.* **211**, 135 (1992)].
12. Actually, the only physical requirement is that friction dissipates energy, such that $\dot{\mathbf{T}}$ integrated over the fault will be less than zero. To our knowledge, the consequences of this less strict requirement have not been reported in the literature.
13. The study of slip weakening and the conditions for spontaneous rupture were introduced in seismology by Y. Ida [*J. Geophys. Res.* **77**, 3796 (1972)], although the conditions had been used in dynamic fracture mechanics [B. Kostrov, L. V. Nikitin, L. M. Flintman, *Mech. Solids* **4**, 112 (1969)]. The friction law used in our simulation is described by A. Palmer and J. Rice [*Proc. R. Soc. London Ser. A* **332**, 527 (1973)] and in the excellent review by J. Rice [in *Physics of the Earth Interior*, A. Dziewonski and E. Boschi, Eds. (North-Holland, Amsterdam, 1980), pp. 555–649]. For a complete review of the relation between seismic faulting and rupture mechanics, see (*2*).
14. Friction should be treated as a vector boundary condition, and our code can handle this. Unfortunately, there is little experimental evidence about the vector properties of friction other than the common assumption that friction is antiparallel to the instantaneous slip rate. For a more detailed discussion, see (*15*).
15. P. Spudich, *Tectonophysics* **211**, 99 (1992).
16. R. Madariaga, K. Olsen, R. Archuleta, in preparation.
17. See the entire collection of papers published in *Bull. Seismol. Soc. Am.* **84** (no. 3) (1994).
18. D. Wald and T. Heaton, *ibid.* **84**, 668 (1994).
19. F. Cotton and M. Campillo, *J. Geophys. Res.* **100**, 3961 (1995).
20. Numerous studies besides (*18*) and (*19*) have analyzed the kinematic rupture parameters of the Landers earthquake, for example, M. Campillo and R. Archuleta [*Geophys. Res. Lett.* **20**, 647 (1993)], B. Cohee and G. Beroza [*Bull. Seismol. Soc. Am.* **84**, 692 (1994)], D. Dreger (*ibid*., p. 713), and R. Abercrombie and J. Mori (*ibid*., p. 725).
21. This method for computing the static stress drop during an earthquake has been used by, among others, T. Miyatake [*Geophys. Res. Lett.* **19**, 349 (1992)], G. Beroza and T. Mikumo [*J. Geophys. Res.* **101**, 22449 (1996)], and T. Mikumo and T. Miyatake [*Bull. Seismol. Soc. Am.* **85**, 178 (1995)].
22. Several investigators have used quasi-dynamic models of recent large earthquakes (*21*). In those pioneering computations, the boundary conditions on the fault were different from ours. In particular, they used the stress excess or Irwin fracture criterion [G. R. Irwin, in *Fracturing of Metals*, F. Jonassen, W. Roop, R. Bayless, Eds. (American Society for Metals, Cleveland, OH, 1947), pp. 147–166] instead of a friction law with an internal length scale (D_0). Irwin's criterion lacks a continuum limit in the sense of J. R. Rice [*J. Geophys. Res.* **98**, 9885 (1993)]. Their numerical resolution was almost two orders of magnitude less than ours, which prevented the inclusion of a length scale in the friction law.
23. For the 1995 Kobe earthquake, D_0 has been estimated to be of the order of 1 m (S. Ide and M. Takeo, in preparation).
24. T. Heaton, *Phys. Earth Planet. Inter.* **64**, 1 (1990).
25. R. Madariaga, K. Olsen, R. Archuleta, *Seismol. Res. Lett.* **68**, 312 (1997).
26. S. Day, *Bull. Seismol. Soc. Am.* **72**, 1881 (1982).
27. The first report of locally supersonic rupture velocities is due to R. Archuleta [*J. Geophys. Res.* **89**, 4559 (1984)], who inverted by trial-and-error accelerograms from the Imperial Valley earthquake, California, 1979. In the temporal reconstruction of the 1992 Landers rupture (magnitude 7.3) (*18*), the rupture velocity varies significantly from start to end. Between 15 and 17.5 s, the rupture velocity is estimated at 4 km/s, which is faster than the fastest *S*-wave velocity of 3.52 km/s in the fault zone used for the source inversion.
28. R. Archuleta and G. Frazier, *Bull. Seismol. Soc. Am.* **68**, 541 (1978).
29. The computations in this study were carried out in part on the SGI Origin 2000 at the Materials Research Laboratory, University of California, Santa Barbara (NSF grant CDA96-01954), and in part on the Sparc20 server at the Institute for Crustal Studies, University of California, Santa Barabara (NSF grant EAR 96-28682), and the Southern California Earthquake Center (SCEC) (USC 572726 through NSF cooperative agreement EAR-8920136). R.M.'s work was supported by the Environment Program of the European Community under Project Strong Ground Motion from Earthquakes. Movies of the Landers earthquake simulation can be found on the World Wide Web at URL http://quake.crustal.ucsb.edu/~kbolsen. This is Institute for Crustal Studies contribution 0272-64EQ and SCEC contribution 383.

21 July 1997; accepted 23 September 1997

Mesoporous Platinum Films from Lyotropic Liquid Crystalline Phases

George S. Attard,* Philip N. Bartlett, Nicholas R. B. Coleman, Joanne M. Elliott, John R. Owen, Jin Hai Wang

The lyotropic liquid crystalline phases of surfactants exhibit a rich polymorphism of structures that have long-range periodicities and whose characteristic repeat distances range from 2 to 15 nanometers. The electrochemical reduction of platinum salts confined to the aqueous environments of these phases leads to the deposition of platinum films that have a well-defined long-ranged porous nanostructure and high specific surface areas. These results suggest that the use of liquid crystalline plating solutions could be a versatile way to create mesoporous electrodes for batteries, fuel cells, electrochemical capacitors, and sensors.

The use of micellar solutions of surfactants in the synthesis of oxide ceramics is currently the subject of considerable research, because the resulting materials, which combine high specific surface areas and larger pore sizes than are achievable in conventional zeolites, are of interest for applications in catalysis and size-selective chemical separations (*1*–*9*). We have shown that the synthesis of nanostructured oxides can also be achieved by using high surfactant concentrations (>30 weight %) (*10*), so that the reaction mixture is in a homogeneous liquid crystalline phase. The advantage of conducting the synthesis in a single phase system is that it is possible to exploit the rich lyotropic polymorphism exhibited by surfactants to produce oxides whose nanostructures are in effect casts of the structures of the liquid crystalline phases in which they were formed. The diversity of periodic nanostructures that is accessible is illustrated by the following examples. Materials synthesized in normal topology hexagonal (H_I) phases have a system of aligned pores disposed on a hexagonal lattice, whereas materials prepared in normal topology cubic (Ia3d) phases have a system of interconnected cylindrical pores that form a gyroid lattice. Similarly, the use of fluid lamellar (L_α) phases produces materials with lamellar nanostructures.

Metals with nanostructures analogous to those of mesoporous oxide ceramics are of considerable interest for applications in catalysis, batteries, fuel cells, capacitors, and sensors (*11*–*14*). Recently we reported that nanostructured platinum can be produced by the chemical reduction of metal salts dissolved in the aqueous domains of a hexagonal lyotropic liquid crystalline phase (*15*). This nanostructured material (which is denoted by H_I-Pt to indicate the phase used in its synthesis) is obtained as a coarse granular material with a specific surface area between 17 and 23 $m^2\ g^{-1}$, which is comparable with that of platinum black (20 to 26 $m^2\ g^{-1}$). Such granular nanostructured metals can be used directly in catalysis, but they are of limited relevance for electrochemical or sensor devices in which the metal is required as a thin film. For those applications, the ability to predetermine the nature of the film's nanostructure through the use of different liquid crystalline phases, together with the control that can be achieved over the characteristic dimensions of the channels, provides new methods for obtaining optimized nanostructures. Here

Department of Chemistry, University of Southampton, Southampton SO17 1BJ, UK.

*To whom correspondence should be addressed. E-mail: gza@soton.ac.uk